remote sensing

MDPI

Article

A Method for Estimating the Aerodynamic Roughness Length with NDVI and BRDF Signatures Using Multi-Temporal Proba-V Data

Mingzhao Yu [1,2], Bingfang Wu [1,*], Nana Yan [1], Qiang Xing [1] and Weiwei Zhu [1]

[1] Key Laboratory of Digital Earth Science, Institute of Remote Sensing and Digital Earth, Chinese Academy of Sciences, Olympic Village Science Park, W. Beichen Road, Beijing 100101, China; yumz@radi.ac.cn (M.Y.); yannn@radi.ac.cn (N.Y.); xingqiang@radi.ac.cn (Q.X.); zhuww@radi.ac.cn (W.Z.)

[2] College of Resources and Environment, University of Chinese Academy of Sciences, Beijing 100049, China

* Correspondence: wubf@radi.ac.cn; Tel.: +86-10-6485-5689

Academic Editors: Clement Atzberger, Mag. Magda Chelfaoui, Jose Moreno and Prasad S. Thenkabail
Received: 25 August 2016; Accepted: 19 December 2016; Published: 24 December 2016

Abstract: Aerodynamic roughness length is an important parameter for surface fluxes estimates. This paper developed an innovative method for estimation of aerodynamic roughness length (z_{0m}) over farmland with a new vegetation index, the Hot-darkspot Vegetation Index (HDVI). To obtain this new index, the normalized-difference hot-darkspot index (NDHD) is introduced using a semi-empirical, kernel-driven bidirectional reflectance model with multi-temporal Proba-V 300-m top-of-canopy (TOC) reflectance products. A linear relationship between HDVI and z_{0m} was found during the crop growth period. Wind profiles data from two field automatic weather station (AWS) were used to calibrate the model: one site is in Guantao County in Hai Basin, in which double-cropping systems and crop rotations with summer maize and winter wheat are implemented; the other is in the middle reach of the Heihe River Basin from the Heihe Watershed Allied Telemetry Experimental Research (HiWATER) project, with the main crop of spring maize. The iterative algorithm based on Monin–Obukhov similarity theory is employed to calculate the field z_{0m} from time series. Results show that the relationship between HDVI and z_{0m} is more pronounced than that between NDVI and z_{0m} for spring maize at Yingke site, with an R^2 value that improved from 0.636 to 0.772. At Guantao site, HDVI also exhibits better performance than NDVI, with R^2 increasing from 0.630 to 0.793 for summer maize and from 0.764 to 0.790 for winter wheat. HDVI can capture the impacts of crop residue on z_{0m}, whereas NDVI cannot.

Keywords: aerodynamic roughness length; HDVI; NDHD; Ross-Li model; Proba-V

1. Introduction

The aerodynamic roughness length (z_{0m}) is defined as the height at which the wind speed becomes zero under neutral conditions [1]. Most currently used land surface models require estimates of aerodynamic roughness length to characterize the momentum transfer between surface and atmosphere [2–4].

The traditional method used to calculate z_{0m} is based on measurements of wind profiles at different levels over the ground under neutral atmospheric conditions, by applying the profile equation derived on the basis of Monin–Obukhov similarity theory [3,5,6]. Typically, according to many long-term observations, modelers have assumed that the momentum roughness is identical at all locations that have similar type of surface coverage [7] and have constructed look-up tables of z_{0m} values over different surfaces [8]. However, these look-up approaches ignore the inherent temporal and spatial variability of a certain land use type and its concomitant effects on momentum transfer [9].

Aerodynamic roughness mainly depends on the geometric features and distributions of the roughness elements [10]. For vegetated surfaces in particular, the mean canopy height, the canopy structure and the plant density are key variables [11]. In the past two decades, remote sensing has emerged as an effective way to retrieve surface information and parameterize aerodynamic roughness on the global or regional scale [12–14], and several models have been developed for z_{0m} as a function of vegetation physical structural parameters, such as leaf area index (LAI) [15,16], canopy area index (CAI) and frontal area index (FAI) [17,18]. Besides, optical parameters such as normalized difference vegetation index (NDVI) estimated by remote sensing have been widely used for z_{0m} estimation [18–21]. For cropland, NDVI is closely correlated with z_{0m} during crop growing period [18,19], Gupta et al. and Moran et al. described the relationship between z_{0m} and NDVI as $z_{0m} = \exp(a + b\ NDVI)$ [20,22].

Nevertheless, the vegetation indexes calculated from single observed angle have limited capacity to retrieve three-dimensional vegetation structures that are closely related to z_{0m}. One potential solution is to bring in multi-angular optical remote sensing [23–26]. Sunlight hitting the vegetation canopy is scattered unevenly because of surface roughness, which is related to the canopy's shape and height. Multi-angular observations can capture the uneven scattering of sunlight by vegetation, which can be described by the bidirectional reflectance distribution function (BRDF) related to the biophysical structural information [24,26–28]. The hotspot-darkspot index (HDS) calculated from multi-angular optical remote-sensing data is capable of representing the geometric structures of vegetation [29]. A high HDS index results from a strong contrast between the hotspot and darkspot reflectances, which is a manifestation of the roughness of the canopy surface [26].

Moreover, the annual variability of crop phenology and daily variability of crop development are major sources of uncertainty for z_{0m} assessments over vegetation. The newly launched Proba-V satellite collects daily reflectance data in the visible and near-infrared (NIR) ranges. The optical design of Proba-V consists of three cameras, providing wide-view angles of $\pm 51^{\circ}$ from nadir that measure abundant directional effects in the surface reflectance. Thus, the BRDF of each pixel can be derived within a few days of observation [30]. Accordingly, this paper aims to develop a new method for estimation of aerodynamic roughness length based on NDVI and BRDF parameters over farmland. The calibration of the new model is done using field-based measurements of wind profiles data from different climate systems.

2. Data and Study Area

2.1. Site Description

In this paper, two sites with typical climates and crop types are selected: the middle reach of the Heihe River Basin with arid climate system in northwestern China and Guantao County with semi-moisture climate system on the North China Plain, Hai basin.

(1) The middle reach of the Heihe River Basin (98°57′–100°52′E, 38°39′–39°59′N) is located in the western part of Gansu Province near Zhangye City, which is the main irrigation agriculture economic zone and main water consumption area in the Heihe River Basin. Figure 1a displays the land-cover classification results in this area determined by Zhong et al. in 2014 using multiple classifiers and multi-source remotely sensed data [31,32]. In recent years, many research projects have addressed land-surface processes, hydrology and water resources, such as HEIFE [33], WATER project [34], and Hi-WATER [35]. Large quantities of ground observation data from meteorological, hydrological and energy flux stations and associated study results have been accumulated, including data from the Yingke automatic weather station (AWS), which were used in this paper (Figure 1b). The Yingke AWS is located in a typical oasis in the middle reach of the Heihe River Basin on very flat terrain and is surrounded by the Gobi Desert. The observational equipment includes a 40-m high tower with the instruments facing north to measure the wind speed, wind direction, atmosphere temperature and temperature humidity at different heights [36]. The main crop near the site is irrigated spring maize, which has a maximum height of approximately 1.8 m [37].

(2) Guantao County is located in the south of Hebei Province in the Hai Basin (115°06′–115°40′ E, 36°27′–36°47′ N) and has a warm temperate, semi-humid, continental monsoon climate. Guantao is a major agricultural county, and the main cultivated crops are winter wheat, maize and cotton. Arable land accounts for 63% of the whole county's area. We created the land-cover map of Guantao County using multi-temporal and high-resolution remote sensing images (GF-1, HJ-1A/1B CCD and TM images), Support vector machine (SVM) was selected for classification with guidance regarding the local crop phonology [38,39] (Figure 2a). The AWS in Guantao was installed with support from the Global Environmental Facility (GEF) Hai Basin project in 2014 (Figure 2b), similar with Yingke site, the equipment on AWS tower includes meteorological sensors installed on different layers. This site is dominated by double crops with the rotation of winter wheat and summer maize (Figure 3).

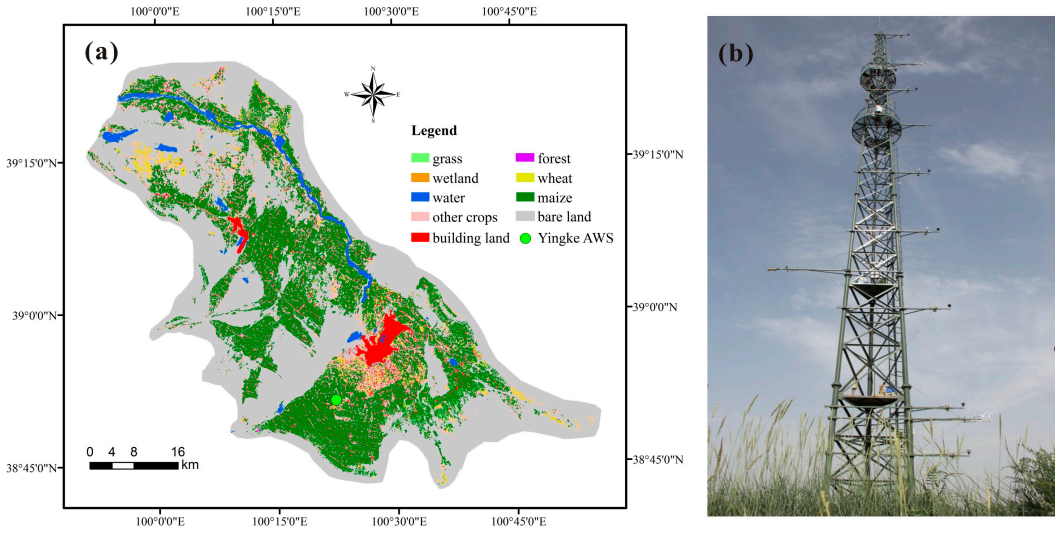

Figure 1. (**a**) Land cover map of the middle reach of the Heihe River Basin in 2014; and (**b**) photograph of the automatic weather station (AWS) tower in Yingke.

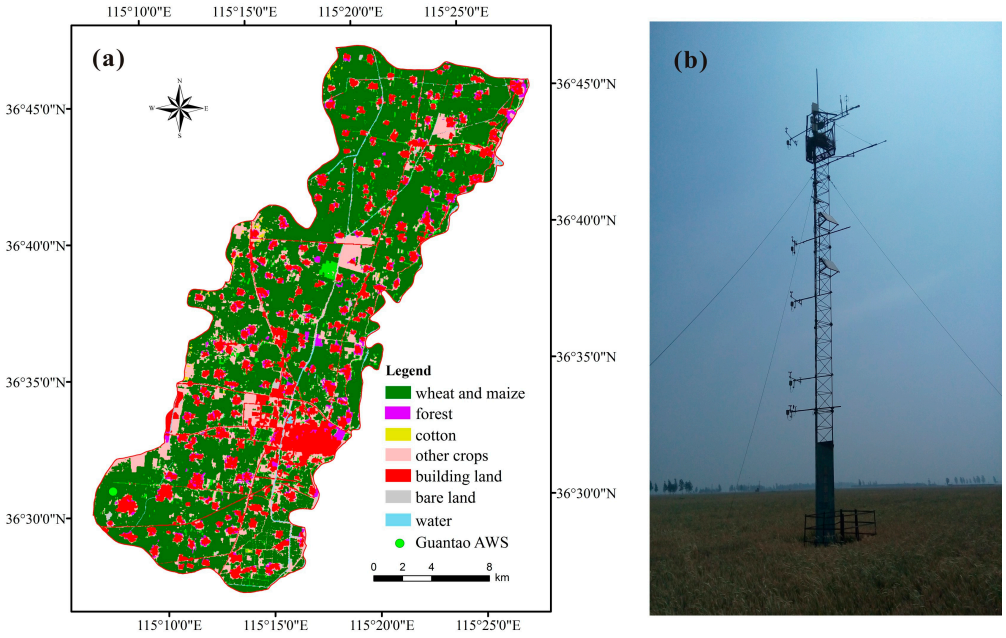

Figure 2. (**a**) Land cover map of Guantao County in 2015; and (**b**) photograph of the AWS tower in Guantao.

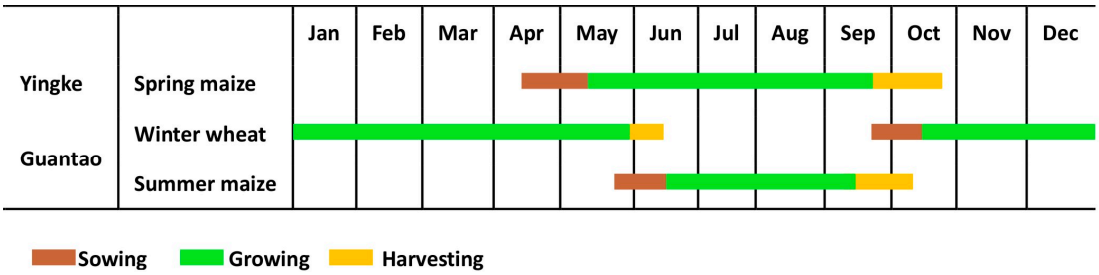

Figure 3. Crop calendars for the Yingke and Guantao Experimental Areas.

2.2. Data

2.2.1. In Situ Data

The AWS systems at these two sites collected data on wind speed, wind direction, air temperature and air humidity at 10-min intervals (Table 1). To guarantee the reliability of the wind profile results, the raw datasets were selected to obtain highly accurate aerodynamic roughness values based on the following criteria: (1) the wind speed is greater than 1 m/s; (2) the wind friction velocity u_* exceeds 0.2 m/s; and (3) data obtained on rainy days are discarded. For further information about the operating principles of the instruments and the data processing, refer to Liu and coworkers' study [35,36].

Table 1. Details about the observation sites.

Location	Coordinates	Land Use	Sensor Height (m)	Period	Data Logger
Yingke	38°51′20″ N, 100°22′20″ E	Spring maize	3, 5, 10, 15, 20, 30, 40	19 May–26 October 2014	CR800
Guantao	36°30′54″ N, 115°7′39″ E	Winter wheat Summer maize	4, 5, 8, 10, 15	15 November 2014–29 May 2015 15 June–15 September 2015	CR1000

2.2.2. Satellite Data

The Proba-V satellite was launched on 6 May 2013 and was designed to bridge the gap in space-borne vegetation measurements between the SPOT-VGT and the upcoming Sentinel-3 satellites. The technical specifications of the on-board sensors on the Proba-V satellite are listed in Tables 2 and 3 [40]. In this study, 300 m daily top-of-canopy (TOC) reflectance products were downloaded from the web page of VITO's Product Distribution Portal (PDP) in HDF5 file format (http://www.vito-eodata.be/).

Table 2. Proba-V 300 m main characteristics.

Local Over Pass Time	10:45
Altitude	820 km
Field of view	102°
Swath width	2295 km

Table 3. Characteristics of Proba-V spectral bands.

Band Name	Spectral Range (μm)	Centre Wavelength (μm)	Geolocation Mean Accuracy (m)
BLUE	0.440–0.487	0.464	60.69
RED	0.614–0.696	0.655	60.46
NIR	0.772–0.902	0.837	61.30
SWIR	1.570–1.635	1.603	61.86

The Proba-V 300 m TOC products were acquired for 2014 in the middle reach of the Heihe River Basin and for 2015 in Guantao based on the crop phenology (Figure 3). Two images (Titles: X27Y03 and X28Y03) were needed to cover the middle reach of the Heihe River Basin, whereas one was sufficient

for Guantao (Titles: X29Y03). The required data groups including the solar zenith angles (SZA), solar azimuth angles (SAA), viewing zenith angles of the visible and NIR (VNIR) detector (VZA), viewing azimuth angles of the VNIR detector (VAA), quality control, and the TOC reflectances of RED and NIR were extracted and converted to image files from the original HDF5 files by Spirits software [41]. The images were mosaicked and clipped to the study area, projected to Albers conical equal area projections, and resampled using the bilinear interpolation method.

3. Methods

3.1. Ground Aerodynamic Roughness Length

The aerodynamic surface roughness length can be determined iteratively based on wind profile data. Using Monin–Obukhov similarity, roughness length and zero-plane displacement can be related via the logarithmic wind profile equation [42]:

$$u = \frac{u_*}{k}\left[\ln\left(\frac{z-d}{z_{0m}}\right) - \Psi_m\left(\frac{z-d}{L}\right)\right], \quad (1)$$

$$\theta = \frac{\theta_*}{k}\left[\ln\left(\frac{z-d}{z_{0h}}\right) - \Psi_h\left(\frac{z-d}{L}\right)\right] + \theta_0, \quad (2)$$

where u and θ are the wind speed and potential air temperature, respectively, at height z above ground level; u_* is the friction velocity; θ_* is the friction temperature; k is von Karman's constant ($k = 0.4$); d is the zero-plane displacement; z_{0m} is the aerodynamic roughness length; z_{0h} is the thermal roughness length; θ_0 is the potential temperature near the surface; L is a function of the friction velocity, friction temperature and temperature (called the Monin–Obukhov length); and Ψ_m and Ψ_h are the stability functions. The expressions of the stability functions Ψ_m and Ψ_h depend on the stability conditions in the surface layer, which are described by the stability parameter Z/L [43].

For $Z/L < 0$ (unstable conditions) [44],

$$\Psi_m = \ln\frac{1+x^2}{2} + 2\ln\frac{1+x}{2} - 2\mathrm{arctg}x + \frac{\pi}{2}, \quad (3)$$

$$\Psi_h = 2\ln\frac{1+y}{2}, \quad (4)$$

$$x = \left(1 - 15\frac{z-d}{L}\right)^{\frac{1}{4}}, \; y = \left(1 - 16\frac{z-d}{L}\right)^{\frac{1}{2}}, \quad (5)$$

For $Z/L > 0$ (stable conditions) [45],

$$\Psi_m = \Psi_h = -5\frac{z-d}{L}, \quad (6)$$

In this study, we use least-square method to determine z_{0m} [46,47]. Equation (1) can be written as the following simplified form:

$$u = ax + b, \quad (7)$$

where $a = u_*/k$, $x = \ln(z-d) - \Psi_m$ and $b = -\ln z_{0m} \cdot a$. Commonly, d has a relationship with the vegetation height (h) that d equals to 0.67 h over surfaces covered by dense and homogeneous vegetation [48], therefore, d is determined through iterative algorithm which increases from 0.1 m to 3 m at intervals of 0.1 m. For each given d, there is a correlation coefficient for the fitting Equation (7), and d is chosen as the optimum value when the correlation coefficient reaches maximum, then, z_{0m} can be calculated according to d value.

3.2. BRDF Parameters with Ross-Li Model

The semi-empirical, kernel-driven BRDF model is generally used to correct BRDF effects and retrieve surface albedo from multi-angle datasets [30,49,50]. This model relies on the weighted sum of an isotropic parameter and two kernels of viewing and the illumination geometry to determine the reflectance of certain observed angles [27]. The Ross–Li–Maignan model is formulated as follows.

$$R(\theta_i, \theta_r, \varphi) = f_{iso}(\lambda) + f_{vol}(\lambda)\, K_{vol}(\theta_i, \theta_r, \varphi) + f_{geo}(\lambda)\, K_{geo}(\theta_i, \theta_r, \varphi), \quad (8)$$

In Equation (8), the surface reflectance (R) is expressed as a function of three components. The relative azimuth is $\varphi = \varphi_i - \varphi_r$. f_{iso} is the reflectance acquired by nadir observation when the solar zenith angle is zero. K_{vol} describes the volume scattering kernel, and K_{geo} describes the surface scattering kernel. Volume scattering is caused by a horizontal layer of randomly distributed leaves, and surface scattering is caused by the shadows of natural objects. These two kernels are functions of only the solar and sensor geometries, including the solar zenith angle (θ_i), view zenith angle (θ_r) and relative azimuth angle (φ). $f_{vol}(\lambda)$ and $f_{geo}(\lambda)$ are the spectrally dependent BRDF kernel coefficients. In this study, K_{vol} and K_{geo} were calculated using the Li-Sparse model and the Ross Thick model, as described by Equations (9) and (11), respectively [28], and ξ, is the phase angle calculated by Equation (12).

$$K_{geo}(\theta_i, \theta_r, \varphi) = \frac{1}{\pi}(t - \sin t \cos t)(\sec\theta_i + \sec\theta_r), \quad (9)$$

$$\cos t = \frac{2\sqrt{\tan^2\theta_i + \tan^2\theta_r - 2\tan\theta_i \tan\theta_r \cos\varphi + (\tan\theta_i \tan\theta_r \sin\varphi)^2}}{\sec\theta_i + \sec\theta_r}, \quad (10)$$

$$K_{vol}(\theta_i, \theta_r, \varphi) = \frac{(\frac{\pi}{2} - \xi)\cos\xi + \sin\xi}{\cos\theta_i + \cos\theta_r} - \frac{\pi}{4}, \quad (11)$$

$$\cos\xi = \cos\theta_i \cos\theta_r + \sin\theta_i \sin\theta_r \cos\varphi, \quad (12)$$

To calculate the kernel coefficients, a multiple linear regression fit was applied with 21-day series of reflectance and angle data. Because the model is relatively insensitive to noisy data [49], here, we use Proba-V's quality control file to determine each pixel's quality flag and, thereby, discard the cloudy and invalid pixels. For a specific pixel, if at least five cloud-free observations of the surface are available during a 21-day period, the kernel coefficients are calculated; otherwise, it is assigned an invalid value. Then, reflectance at any angle can be acquired in the hemisphere.

3.3. NDHD, NDVI and HDVI

In the principal plane, the reflectance exhibits large variations at different scattering angles. This information is very useful for measuring the canopy structure. The largest reflectance in the principal plane is chosen as the hot spot, and the smallest defined as the dark spot where shadows created by the vegetation canopy are maximally observed [24]. In practice, usually we cannot obtain both hotspot and darkspot directly on the simulated curve as shown in Figure 4, so the darkspot (hotspot) is defined at the same view zenith angle with the hotspot (darkspot) but in the forward-scattering (back-scattering) direction, in order to extract the hotspot reflectance (ρ_{HS}) and the darkspot reflectance (ρ_{DS}). As Leblanc et al. proposed in 2001 [51], the normalized-difference hotspot-darkspot index (NDHD) is the normalized difference between ρ_{HS} and the ρ_{DS}:

$$NDHD = \frac{\rho_{HS} - \rho_{DS}}{\rho_{HS} + \rho_{DS}}, \quad (13)$$

The normalized index selected for this research is to reduce the influence of canopy optical properties and enhance the importance of canopy structure. Analogously, the HDS index ($(\rho_{HS} - \rho_{DS})/\rho_{DS}$), which was proposed by Lacaze et al. [29], has been widely used in recent research.

For HDS, the problem of mixed pixels becomes prominent at Proba-V's 300 m resolution: Some pixels containing mixed cropland and bare land demonstrate low ρ_{DS} values, resulting in abnormal HDS values. Therefore, NDHD was applied here.

Daily NDVI images are generated from Proba-V's RED and NIR bands. Based on the quality control file, time series of 5-day composite NDVI at 300 m resolution are acquired to reduce the disturbance of cloudy pixels. Unlike the reflectance, the use of NDVI partially avoids the impact of BRDF signatures because the directional effects are similar in the visible and NIR bands, and therefore, the effect on the individual reflectances can be reduced by taking the ratio of the two bands [52]. However, BRDF signatures, such as the NDHD, can express z_{0m} according to the point on the canopy structure, whereas NDVI cannot. Because both NDVI and NDHD are positively correlated with z_{0m} but their correlations rely on different aspects, a new vegetation index, the Hot-darkspot Vegetation Index (HDVI), which combines NDVI and NDHD is proposed and defined by Equation (14).

$$\mathrm{HDVI} = \mathrm{NDVI} \times (1 + \mathrm{NDHD}), \tag{14}$$

A linear relationship between HDVI and z_{0m} was attempted to map z_{0m} as follows.

$$z_{0m} = a \times \mathrm{HDVI} + b, \tag{15}$$

4. Results

4.1. Simulated Reflectance in Red and NIR Band

As shown in Figure 4, the pixel at which the Yingke station is located is taken as an example to demonstrate the simulated changes in the reflectances of the red and NIR bands in Proba-V's field of view. The solar zenith angle is fixed at 35 degrees in the principal plane. Based on the calendar of Yingke's maize, the first day of each crop-growing month is selected for this example.

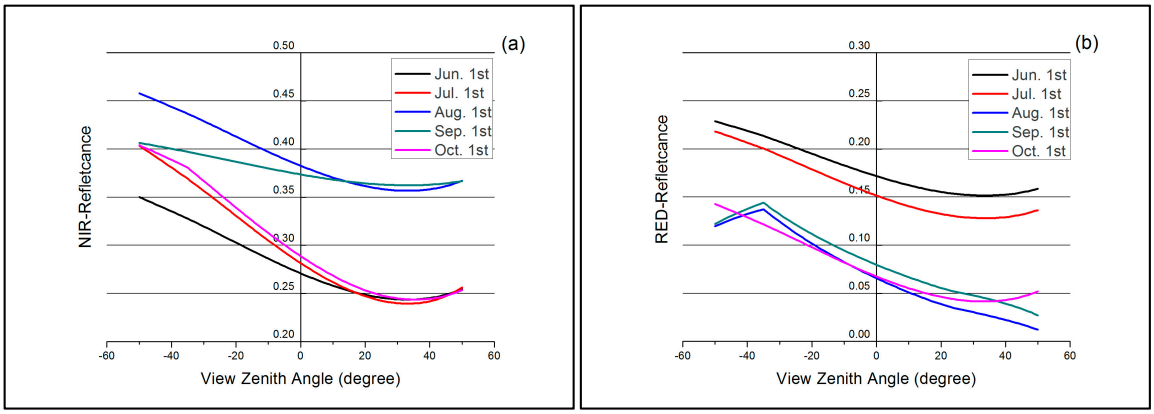

Figure 4. Simulated: (**a**) near-infrared (NIR); and (**b**) RED reflectances at Yingke station according to changes in the view zenith angle on the first day of the month, for five months.

This figure shows that the reflectances of the two channels exhibit a decreasing trend from the back-scattering region to the forward-scattering region. The lowest point, which is known as the darkspot, can be identified on most curves as the point at which the view zenith angle is the same as the solar zenith angle. The hotspot did not appear in the simulated range of the view zenith angle, and the darkspot did not appear on the red-reflectance curves on 1 August and 1 September.

The NDHD of the NIR reflectance varies regularly with the crop growth period, with high values during the initial and terminal stages of crop growth and low values during the vigorous growth stage, in response to the variation of the crop-canopy structures. In contrast, the NDHD of RED reflectance

exhibits less variation (the nearly identical inclination of the five curves in Figure 4b) during the crop growth period, and thus, we calculate the NDHD by applying the NIR band.

4.2. Relationship between NDVI/HDVI and z_{0m}

As shown in Figure 3, the growing season of spring maize in the Yingke Site is from May to October. In this paper, daily averaged aerodynamic roughness values are calculated from AWS raw data with 10-min intervals. To match the NDVI data, the mean value of z_{0m} is obtained over five days with the assumption that z_{0m} changed little during that period.

For the Yingke site, the temporal variations of the aerodynamic roughness, as deduced from the values for each five-day period, reflect the process of crop growth, which exhibits a characteristic rise and fall according to the crop growth cycle (Figure 5). The NDVI values are low at the beginning of crop emergence and increase rapidly over the course of the subsequent month. The peak growth stage lasts 184–244 days. Then, the NDVI values decrease as the spring maize approaches maturity. Clearly, the variations of NDVI are in good agreement with those of z_{0m}, suggesting that NDVI is a reasonable predictor of z_{0m}. Compared with the NDVI profile during the maize growth period, the changing trend of NDHD generally exhibited almost opposite directions, initially increasing rapidly and maintaining a high level from Days 264 to 299.

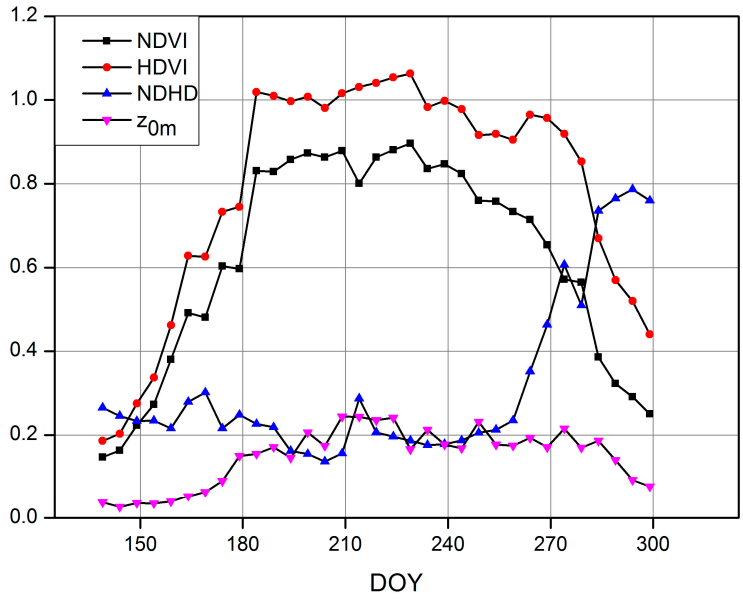

Figure 5. Time series profiles of NDVI, HDVI, NDHD and field observed z_{0m} during the spring maize growing season at Yingke site in 2014. z_{0m} is presented as a five-day average, and NDVI is shown as the maximum value over five days. NDHD and HDVI were calculated with Equations (15) and (16), respectively.

Figure 6 reports the field-observed aerodynamic roughness (z_{0m}), plotted as linear functions of NDVI and HDVI in the Yingke Site. This figure clearly demonstrates that the NDVI of arable land is correlated with z_{0m} ($R^2 = 0.636$, n = 33). In contrast, the data are less dispersed and the correlation is higher ($R^2 = 0.793$, n = 33) when z_{0m} is plotted as a function of HDVI (Figure 6b). In addition, the NDVI and HDVI values in October (points from A~F in Figure 6) exhibit obviously different correlations with z_{0m}: For the same value of z_{0m}, NDVI showed much greater deviation from the fitted curve, while HDVI was distributed around the fitted curve for the six marked points. This finding indicates that NDVI decreased quickly with z_{0m} during the crop harvesting stage when the leaf cells of spring maize senesce, and the leaves become yellow and withered, resulting in z_{0m} less evaluated if only

the changes of NDVI were taken into concern. In contrast, HDVI, which contains information on the crop-planting structure, has advantages for retrieving z_{0m} in the late growth period.

The same method was used to determine the differences between NDVI and HDVI for winter wheat and summer maize at the Guantao site. The linear fitting equations based on the crop calendar of Guantao are shown in Figure 7. The R^2 values of the four fitted equations also indicate that HDVI is more significantly correlated with z_{0m} than NDVI. Comparable results are also obtained for the relationships of z_{0m} of Guantao's summer maize and NDVI/HDVI, with the correlation coefficient improving from 0.670 to 0.793. The HDVI-based model produces a slightly better fitting result than the NDVI-based model (the R^2 value ranges from 0.764 to 0.790) for winter wheat in Guantao.

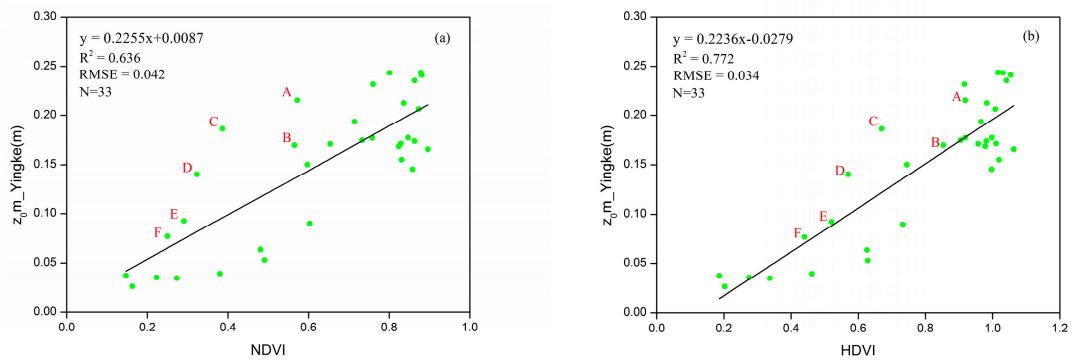

Figure 6. Observed aerodynamic roughness length as functions of: (**a**) NDVI; and (**b**) HDVI. The data were collected during the growth period of spring maize (April to October) in 2014 at the Yingke site. Points A–F represent the values for October 1, 6, 11, 16, 21 and 26, respectively.

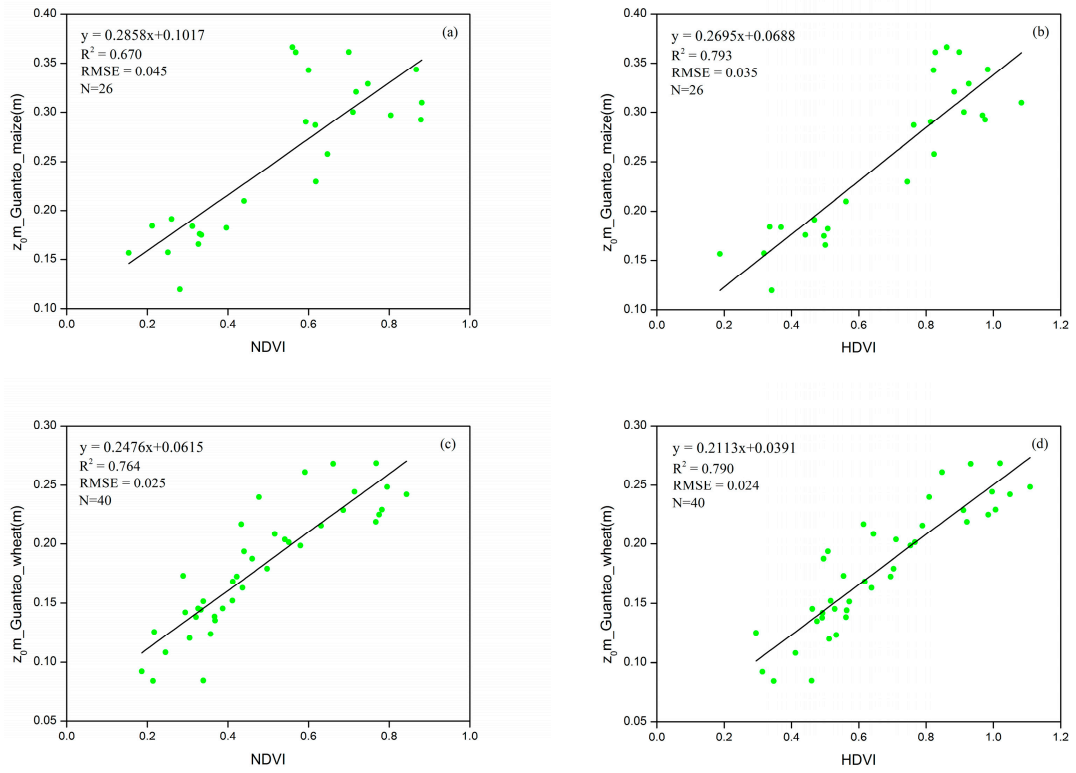

Figure 7. Observed aerodynamic roughness length as a function of: (**a**) the NDVI of summer maize; (**b**) the HDVI of summer maize; (**c**) the NDVI of winter wheat; and (**d**) the HDVI of winter wheat. The data were selected according to the growth period of the specific crop at the Guantao site.

Coefficients a and b of Equation (14) are acquired for different crop types from the linear fitting results shown in Figures 6 and 7 at the Yingke site and the Guantao site, respectively. The results are shown in Table 4, along with the coefficients of determination (R^2). The robustness of z_{0m} model performance is evaluated using the root mean square error (RMSE) and the mean absolute error (MAE), which can measure the accuracy of the established model. The RMSE and MAE values between the observed z_{0m} and estimated z_{0m} for different crops range from 0.024 to 0.035 and from 0.020 to 0.028, respectively, which are lower than 0.1, indicating consistency between the observed z_{0m} and HDVI-based estimated z_{0m}. In particular, Durbin–Watson statistics are generally lower than 2, indicating that the error terms are positively auto-correlated. Results of the F-test suggest that the fitted models with *p*-values lower than 0.01, indicating a significant relationship between HDVI/NDVI data and field observed z_{0m} at the 99% confidence level for all crops, confirming the strong capability of the model.

Table 4. The coefficients used to calculate z_{0m} for different crop types and statistical results.

Location	**Yingke**		**Guantao**			
Crop Type	Spring Maize		Winter Wheat		Summer Maize	
Number of points	33		40		26	
Correlation with z_{0m}	HDVI	NDVI	HDVI	NDVI	HDVI	NDVI
a	0.2236	0.2255	0.2113	0.2476	0.2695	0.2858
b	−0.0279	0.0087	0.0391	0.0615	0.0688	0.1017
R^2	0.772	0.636	0.790	0.764	0.793	0.670
RMSE	0.034	0.042	0.024	0.025	0.035	0.045
MAE	0.027	0.031	0.020	0.018	0.028	0.033
Durbin-Watson statistic	1.338	0.927	1.821	1.778	1.611	1.250
F-statistics	15.435	12.734	17.827	12.550	11.034	8.370
***p*-value**	4.39×10^{-12}	6.48×10^{-11}	8.22×10^{-16}	3.97×10^{-13}	3.31×10^{-8}	5.74×10^{-7}

4.3. Regional-Scale z_{0m}

We use the relationship between HDVI and the aerodynamic roughness length z_{0m} to derive maps of the roughness length. To explore the seasonal and spatial variability of the aerodynamic roughness, we focus on the middle reach of the Heihe River Basin and estimate z_{0m} over the spring maize mask [31,32] of certain days from May to October, as shown in Figure 8. The value of z_{0m} ranges between 0 and 0.25 throughout the spring maize growing season in this area, reaches a peak in July and then declines beginning in August when the height of the maize plants reaches a plateau. The largest standard deviation value of all maize pixels occurred in June, indicating that z_{0m} exhibited more significant spatial differentiation during this period. This is most likely attributable to spatial differences in the sowing time, planting density and fertilization method of spring maize. The differences are also amplified by the rapid growth that occurs during this stage.

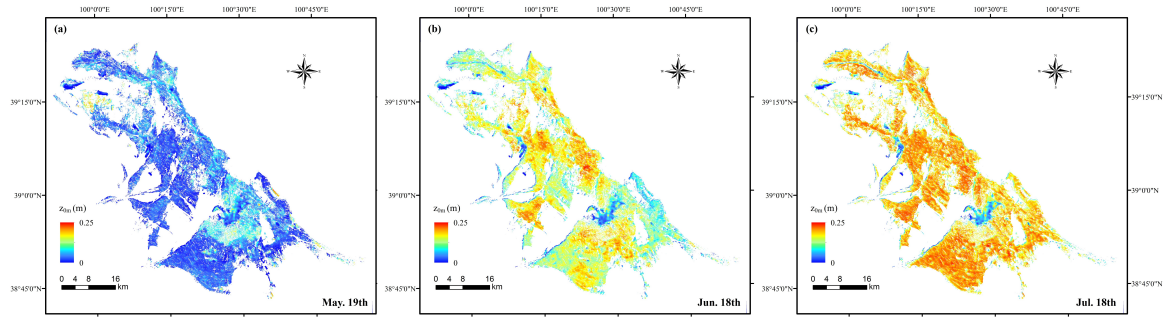

Figure 8. *Cont.*

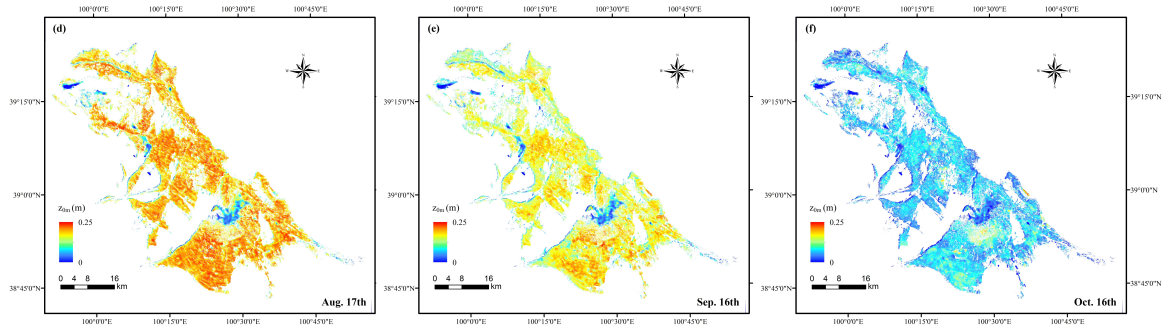

Figure 8. Estimated aerodynamic roughness lengths of spring maize in the middle reach of the Heihe River Basin on: (**a**) 19 May; (**b**) 18 June; (**c**) 18 July; (**d**) 17 August; (**e**) 16 September; and (**f**) 16 October.

5. Discussion

With the development of remote-sensing technology, satellite-based algorithms are now routinely applied to retrieve terrestrial parameters, such as aerodynamic roughness. Because vegetation height is essential in most aerodynamic roughness models, usually field investigation or indirect methods are needed to acquire the spatial distribution of the vegetation height. Here, we try to wean the vegetation height observation off by developing a purely remote-sensing-based model for aerodynamic roughness estimation over arable land, improving the timeliness put forward for aerodynamic roughness. The introduction of BRDF signatures improves the accuracy and persuasiveness of the model because the multi-angle remote-sensing data have incomparable advantages for describing the crop canopy structure.

Because crops growing on farmland are flat and uniformly distributed, the topographic changes can be ignored, and the aerodynamic roughness can be separated into two parts: vertical roughness associated with crop growth conditions and horizontal roughness associated with crop planting structures. NDVI still plays the leading role in reflecting crop growth conditions, and NDHD expresses the variations in the vegetation spatial structure. Satisfactory results for aerodynamic roughness length estimation were obtained. According to our results, HDVI clearly exhibits better performance for aerodynamic roughness estimation than NDVI. Compared with NDVI, HDVI's range is wider, and it can exceed 1. The exponential algorithm describing z_{0m} [21,23] can be improved with linear model after the introduction of NDHD.

According to the results shown in Figures 6 and 7, this method is more efficient for maize than wheat. This finding can be explained by two reasons: (1) Wheat plants grow to approximately the same height and are usually closely spaced. Thus, the canopy of wheat is more flat and homogeneous than that of maize, and the spatial heterogeneity of wheat land, which affects the NDHD, changes less during the crop growth period. (2) The differences in the crop ripening stage and harvest period for the two crops may affect the results. Typically, maize stalk residues remain quite tall and are sparsely distributed over farmland after harvest (Figure 9a), as reflected by higher NDHD values. However, NDVI is difficult to interpret at this stage. For wheat, the approximate height of the residue is only 30 cm (Figure 9b). Therefore, the canopy structure is similar to that of bare land, and few BRDF signatures are captured by the NDHD. Thus, the plant structures and growth characteristics of different crops should be considered when modeling z_{0m}.

The method discussed here only applies to two crops (wheat and maize), because the aerodynamic roughness of different land use types differ significantly (by as much as orders of magnitude) [53,54]. Results are based on limited datasets under particular meteorological conditions. Further research is needed to determine the model's applicability to other crop and vegetation types. This study was limited by inadequate AWS data for different underlying surface types. Although eddy covariance (EC) and large-aperture scintillometer (LAS) measurements have been used to acquire local roughness length values in previous studies [55,56], the estimation of z_{0m} using different instruments may

introduce deviations in the same region because of the differences among AWS, EC and LAS footprints. The consistency and precision of ground data constitute the foundation of modeling based on remote sensing data. In our study, the two AWS sites were located in homogeneous and flat arable land; thus, the observed z_{0m} values are representative of the corresponding remote-sensing pixels, and the impact of topographic fluctuation is avoided. Actually, the surface condition of the vegetation cover is not the only factor that must be considered. The near-ground wind speed, wind direction and stability conditions also strongly influence the aerodynamic roughness [55,57]. In our study, meteorological conditions were not accounted for, which may have affected the fitting results for the field-observed z_{0m} and HDVI. The effects of wind speed and wind direction on z_{0m} should be studied further, moreover, boundary layer conditions also play a role in surface-atmosphere exchanges parameterized through z_{0m}. It should be noted, however, that high-resolution surface meteorological data acquisition is also a key problem in determining the spatial distribution of z_{0m}.

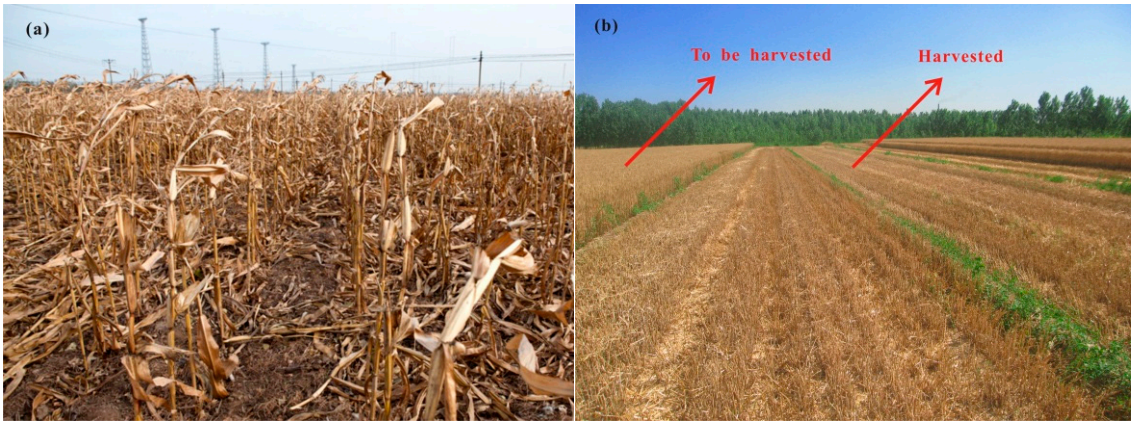

Figure 9. Photographs of: (**a**) maize residue; and (**b**) wheat residue.

Proba-V was designed to offer global coverage at spatial resolutions of 100 m, 300 m and 1 km [40]. The 300 m TOC reflectance products used here can facilitate the observation of a certain terrestrial target on a daily basis in most locations on Earth. Similar to the angular observations collected by the Moderate Resolution Imaging Spectroradiometer (MODIS) instrument [49], multi-temporal data are extracted from a series of Proba-V passes. The BRDF model parameters were derived from the observed time series. Regression of the semi-empirical kernel-driven BRDF model should be performed over sub-periods that are short enough that the surface can be considered time invariant and long enough to contain sufficient sensor data for the regression [27]. Obtaining sufficient cloud-free surface reflectance data is challenging over certain regions. The main limitation of this method is the assumption that the target is stable during the synthesis period. This assumption is obviously invalid for vegetation-covered land. Thus, we must assume that the variations in the BRDF shape are limited, so the period of 21 days was set for regression with multi-temporal Proba-V images to ensure the accuracy of the BRDF signatures. Consequently, multi-angular optical remote-sensing platforms with high spatial resolution and short revisit periods are still needed to further advance this research. Additionally, in the future, attempts to acquire multi-angular data from multi-source remote sensing data should be made.

6. Conclusions

This paper proposed a new model for estimating z_{0m} over arable land with a new vegetation index, the Hot-darkspot Vegetation Index (HDVI) with multi-temporal Proba-V 300-m TOC reflectance products. The linear relationship between HDVI and z_{0m} was found for the crop growth period. The results show that the relationship between HDVI and z_{0m} is more pronounced than that between NDVI and z_{0m} for spring maize at the Yingke site, with an R^2 value that improved from 0.636 to 0.772.

At the Guantao site, in which double-cropping systems and crop rotations with summer maize and winter wheat are implemented, HDVI also exhibits better performance than NDVI, with R^2 increasing from 0.630 to 0.793 for summer maize and from 0.764 to 0.790 for winter wheat. The differences probably originate from the crop ripening stage and harvest period, indicating crop residue's impacts on z_{0m} captured by NDHD, when NDVI makes little sense to crop at that stage. NDHD from near-infrared reflectance contains more meaningful BRDF information associated with canopy structure against red reflectance. However, this study was based on limited available data, HDVI will be adopted and qualified over different vegetation types in long periods of time with the accumulation of robust validation exercise.

Acknowledgments: This work was supported in part by Advanced Science Foundation Research Project of the Chinese Academy of Sciences (Grant No.: QYZDY-SSW-DQC014) and the Natural Science Foundation of China, Grant No. 41271424 and No. 41501479. We thank VITO for providing the Proba-V 300 m products. The authors also thank the Environmental and Ecological Science Data Center for West China, National Natural Science Foundation of China for providing the AWS data and land cover map (http://westdc.westgis.ac.cn).

Author Contributions: Mingzhao Yu contributed to the research experiments, analyzed the data, and wrote the paper. Bingfang Wu conceived the experiments, and was responsible for the research analysis. Nana Yan, Qiang Xing and Weiwei Zhu collected and pre-processed the original data. All the co-authors helped to revise the manuscript.

Conflicts of Interest: The authors declare no conflict of interest.

References

1. Su, Z.; Schmugge, T.; Kustas, W.P.; Massman, W.J. An evaluation of two models for estimation of the roughness height for heat transfer between the land surface and the atmosphere. *J. Appl. Meteorol.* **2001**, *40*, 1933–1951. [CrossRef]
2. Liou, Y.A.; Galantowicz, J.F.; England, A.W. A land surface process/radio brightness model with coupled heat and moisture transport for prairie grassland. *J. IEEE Trans. Geosci. Remote Sens.* **1999**, *37*, 1848–1859. [CrossRef]
3. Hryama, T.; Sugita, M.; Kotoda, K. Regional roughness parameters and momentum fluxes over a complex area. *J. Appl. Meteorol.* **1996**, *35*, 2179–2190. [CrossRef]
4. Marticorena, B.; Kardous, M.; Bergametti, G.; Callot, Y.; Chazette, P.; Khatteli, H.; Le Hégarat-Mascle, S.; Maillé, M.; Rajot, J.; Vidal-Madjar, D.; et al. Surface and aerodynamic roughness in arid and semiarid areas and their relation to radar backscatter coefficient. *J. Geophys. Res. Earth Surf.* **2006**, *111*. [CrossRef]
5. Monteith, J.L. The micrometeorology of crops. In *Principles of Environmental Physics*; Edward Arnold: London, UK, 1973; pp. 190–215.
6. Brutsaert, W. *Evaporation into the Atmosphere. Theory, History, and Applications*; Springer: Dordrecht, The Netherlands, 1982.
7. Chen, F.; Mitchell, K.; Schaake, J.; Xue, Y.; Pan, H.; Koren, V.; Duan, Q.Y.; Ek, M.; Betts, A. Modeling of land surface evaporation by four schemes and comparison with FIFE observations. *J. Geophys. Res. Atmos.* **1996**, *101*, 7251–7268. [CrossRef]
8. Allen, R.G.; Tasumi, M.; Morse, A.; Trezza, R.; Wright, J.L.; Bastiaanssen, W.; Kramber, W.; Lorite, I.; Robison, C.W. Satellite-based energy balance for mapping evapotranspiration with internalized calibration (METRIC)–Model. *J. Irrig. Drain. Eng.* **2007**, *133*, 395–406. [CrossRef]
9. Borak, J.S.; Jasinski, M.F.; Crago, R.D. Time series vegetation aerodynamic roughness fields estimated from MODIS observations. *Agric. For. Meteorol.* **2005**, *135*, 252–268. [CrossRef]
10. Maurer, K.D.; Hardiman, B.S.; Vogel, C.S.; Bohrer, G. Canopy-structure effects on surface roughness parameters: Observations in a Great Lakes mixed-deciduous forest. *Agric. For. Meteorol.* **2013**, *177*, 24–34. [CrossRef]
11. Jasinski, M.F.; Crago, R.D. Estimation of vegetation aerodynamic roughness of natural regions using frontal area density determined from satellite imagery. *Agric. For. Meteorol.* **1999**, *94*, 65–77. [CrossRef]
12. Hasager, C.B.; Jensen, N.O. Surface-flux aggregation in heterogeneous terrain. *Q. J. R. Meteorol. Soc.* **1999**, *125*, 2075–2102. [CrossRef]

13. Menenti, M.; Ritchie, J.C.; Humes, K.S.; Parry, R.; Pachepsky, Y.; Gimenez, D.; Leguizamon, S. Estimation of aerodynamic roughness at various spatial scales. In *Scaling up in Hydrology Using Remote Sensing*; John Wiley and Sons: Chichester, UK, 1996; Volume 272.
14. Menenti, M.; Ritchie, J.C. Estimation of effective aerodynamic roughness of walnut gulch watershed with laser altimeter measurements. *Water Resour. Res.* **1994**, *30*, 1329–1337. [CrossRef]
15. Choudhury, B.J.; Monteith, J.L. A four-layer model for the heat budget of homogeneous land surfaces. *Q. J. R. Meteorol. Soc.* **1988**, *114*, 373–398. [CrossRef]
16. Myneni, R.B.; Hoffman, S.; Knyazikhin, Y.; Privette, J.L.; Glassy, J.; Tian, Y.; Wang, Y.; Song, X.; Zhang, Y.; Smith, G.R.; et al. Global products of vegetation leaf area and fraction absorbed PAR from year one of MODIS data. *Remote Sens. Environ.* **2002**, *83*, 214–231. [CrossRef]
17. Raupach, M.R. Simplified expressions for vegetation roughness length and zero-plane displacement as functions of canopy height and area index. *Bound. Layer Meteorol.* **1994**, *71*, 211–216. [CrossRef]
18. Schaudt, K.; Dickinson, R.E. An approach to deriving roughness length and zero-plane displacement height from satellite data, prototyped with BOREAS data. *Agric. For. Meteorol.* **2000**, *104*, 143–155. [CrossRef]
19. Li, J.; Wang, J.; Menenti, M. Estimation of area roughness length for momentum using remote sensing data and measurements in field. *Sci. Atmos. Sin.* **1999**, *23*, 632–640.
20. Gupta, R.K.; Prasad, T.S.; Vijayan, D. Estimation of roughness length and sensible heat flux from WiFS and NOAA AVHRR data. *Adv. Space Res.* **2002**, *29*, 33–38. [CrossRef]
21. Zhang, J.; Huang, J.P.; Zhang, Q. Retrieval of aerodynamic roughness length character over sparse vegetation region. *Acta Ecol. Sin.* **2010**, *30*, 2819–2827.
22. Moran, M.S.; Clarke, T.R.; Inoue, Y.; Vidal, A. Estimating crop water deficit using the relation between surface-air temperature and spectral vegetation index. *Remote Sens. Environ.* **1994**, *49*, 246–263. [CrossRef]
23. Chen, J.M.; Liu, J.; Leblanc, S.G.; Lacaze, R.; Roujean, J. Multi-angular optical remote sensing for assessing vegetation structure and carbon absorption. *Remote Sens. Environ.* **2003**, *84*, 516–525. [CrossRef]
24. Gao, F.; Schaaf, C.B.; Strahler, A.H. Detecting vegetation structure using a kernel-based BRDF model. *Remote Sens. Environ.* **2003**, *86*, 198–205. [CrossRef]
25. De Colstoun, E.C.; Walthall, C.L. Improving global scale land cover classifications with multi-directional POLDER data and a decision tree classifier. *Remote Sens. Environ.* **2006**, *100*, 474–485. [CrossRef]
26. Hasegawa, K.; Matsuyama, H.; Tsuzuki, H.; Sweda, T. Improving the estimation of leaf area index by using remotely sensed NDVI with BRDF signatures. *Remote Sens. Environ.* **2010**, *114*, 514–519. [CrossRef]
27. Roujean, J.L.; Leroy, M.; Deschamps, P.Y. A bidirectional reflectance model of the Earth's surface for the correction of remote sensing data. *J. Geophys. Res. Atmos.* **1992**, *97*, 20455–20468. [CrossRef]
28. Wanner, W.; Li, X.; Strahler, A.H. On the derivation of kernels for kernel-driven models of bidirectional reflectance. *J. Geophys. Res. Atmos.* **1995**, *100*, 21077–21089. [CrossRef]
29. Lacaze, R.; Chen, J.M.; Roujean, J.L. Retrieval of vegetation clumping index using hot spot signatures measured by POLDER instrument. *Remote Sens. Environ.* **2002**, *79*, 84–95. [CrossRef]
30. Schaaf, C.B.; Gao, F.; Strahler, A.H.; Lucht, W.; Li, X.; Tsang, T.; Strugnell, N.C.; Zhang, X.; Jin, Y.; Muller, J.; et al. First operational BRDF, albedo nadir reflectance products from MODIS. *Remote Sens. Environ.* **2002**, *83*, 135–148. [CrossRef]
31. Zhong, B.; Ma, P.; Nie, A.; Yang, A.; Yao, Y.; Lü, W.; Zhang, H.; Liu, Q. Land cover mapping using time series HJ-1/CCD data. *Sci. China Earth Sci.* **2014**, *57*, 1790–1799. [CrossRef]
32. Zhong, B.; Yang, A.; Nie, A.; Yao, Y.; Zhang, H.; Wu, S.; Liu, Q. Finer resolution land-cover mapping using multiple classifiers and multisource remotely sensed data in the Heihe river basin. *IEEE J. Sel. Top. Appl. Earth Obs. Remote Sens.* **2015**, *8*, 4973–4992. [CrossRef]
33. Gao, Y.; Hu, Y. *Advances in HEIFE Research (1987–1994)*; China Meteorological Press: Beijing, China, 1994.
34. Li, X.; Li, X.W.; Li, Z.; Ma, M.; Wang, J.; Xiao, Q.; Liu, Q.; Che, T.; Chen, E.; Yan, G.; et al. Watershed allied telemetry experimental research. *J. Geophys. Res. Atmos.* **2009**, *114*, 2191–2196. [CrossRef]
35. Liu, X.; Cheng, G.D.; Liu, S.M.; Xiao, Q.; Ma, M.; Jin, R.; Che, T.; Liu, Q.; Wang, W.; Qi, Y.; et al. Heihe watershed allied telemetry experimental research (Hiwater): Scientific objectives and experimental design. *Bull. Am. Meteorol. Soc.* **2013**, *94*, 1145–1160. [CrossRef]
36. Liu, S.M.; Xu, Z.W.; Wang, W.Z.; Jia, Z.Z.; Zhu, M.J.; Bai, J.; Wang, J.M. A comparison of eddy-covariance and large aperture scintillometer measurements with respect to the energy balance closure problem. *Hydrol. Earth Syst. Sci.* **2011**, *15*, 1291–1306. [CrossRef]

37. Zhu, W.; Wu, B.; Yan, N.; Feng, X.; Xing, Q. A method to estimate diurnal surface soil heat flux from MODIS data for a sparse vegetation and bare soil. *J. Hydrol.* **2014**, *511*, 139–150. [CrossRef]
38. Zhang, M.; Li, Q.; Wu, B. Investigating the capability of multi-temporal landsat images for crop identification in high farmland fragmentation regions. In Proceedings of the 2012 First International Conference on Agro-Geoinformatics (Agro-Geoinformatics), Shanghai, China, 2–4 August 2012.
39. Jia, K.; Wu, B.; Li, Q. Crop classification using HJ satellite multispectral data in the North China Plain. *J. Appl. Meteorol.* **2013**, *7*, 073576. [CrossRef]
40. Dierckx, W.; Sterckx, S.; Benhadj, I.; Livens, S.; Duhoux, G.; Van Achteren, T.; Francois, M.; Mellab, K.; Saint, G. PROBA-V mission for global vegetation monitoring: Standard products and image quality. *Int. J. Remote Sens.* **2014**, *35*, 2589–2614. [CrossRef]
41. Eerens, H.; Haesen, D. SPIRITS User Manual, v1.4. Available online: http://spirits.jrc.ec.europe.eu/ (accessed on 20 March 2016).
42. Brutsaert, H.W. Exchange processes at the earth-atmosphere interface. In *Engineering Meteorology*; Plate, E., Ed.; Elsevier: New York, NY, USA, 1982; pp. 319–369.
43. Panofsky, H.A. Determination of stress from wind and temperature measurements. *Q. J. R. Meteorol. Soc.* **1963**, *89*, 85–94. [CrossRef]
44. Dyer, A.J. A review of flux-profile relationships. *Bound. Layer Meteorol.* **1974**, *7*, 363–372. [CrossRef]
45. Webb, E.K. Profile relationships: The log-linear range, and extension to strong stability. *Q. J. R. Meteorol. Soc.* **1970**, *96*, 67–90. [CrossRef]
46. Frangi, J.P.; Richard, D.C. The WELSONS experiment: Overview and presentation of first results on the surface atmospheric boundary-layer in semiarid Spain. *Ann. Geophys.* **2000**, *18*, 365–384. [CrossRef]
47. Zhou, Y.; Ju, W.; Sun, X.; Wen, X.; Guan, D. Significant decrease of uncertainties in sensible heat flux simulation using temporally variable aerodynamic roughness in two typical forest ecosystems of China. *J. Appl. Meteorol. Climatol.* **2012**, *51*, 1099–1110. [CrossRef]
48. Pielke, R.A.S. *Mesoscale Meteorological Modeling*, 3rd ed.; Academic Press: San Diego, CA, USA, 2013.
49. Lucht, W.; Schaaf, C.B.; Strahler, A.H. An algorithm for the retrieval of albedo from space using semiempirical BRDF models. *IEEE Trans. Geosci. Remote Sens.* **2000**, *38*, 977–998. [CrossRef]
50. Strugnell, N.C.; Lucht, W. An algorithm to infer continental-scale albedo from AVHRR data, land cover class, and field observations of typical BRDFs. *J. Clim.* **2001**, *14*, 1360–1376. [CrossRef]
51. Leblanc, S.G.; Chen, J.M.; White, H.P.; Cihlar, J.; Roujean, J.L.; Lacaze, R. Mapping vegetation clumping index from directional satellite measurements. In Proceedings of the 8th International Symposium Physical Measurements & Signatures in Remote Sensing, Aussois, France, 8–12 January 2001; pp. 450–459.
52. Holben, B.; Fraser, R.S. Red and near-infrared sensor response to off-nadiir viewing. *Int. J. Remote Sens.* **1984**, *5*, 145–160. [CrossRef]
53. Stull, R.B. *An Introduction to Boundary Layer Meteorology*; Springer Science & Business Media: Dordrecht, The Netherlands, 2012.
54. Liu, X.P.; Dong, Z.B. Review of aerodynamic roughness length. *J. Desert Res.* **2003**, *23*, 337–346. (In Chinese)
55. Chen, Q.; Jia, L.; Hutjes, R.; Menenti, M. Estimation of aerodynamic roughness length over oasis in the Heihe River Basin by utilizing remote sensing and ground Data. *Remote Sens.* **2015**, *7*, 3690–3709. [CrossRef]
56. Sun, G.; Hu, Z.; Wang, J.; Xie, Z.; Lin, Y.; Huang, F. Upscaling analysis of aerodynamic roughness length based on in situ data at different spatial scales and remote sensing in north Tibetan Plateau. *Atmos. Res.* **2016**, *176*, 231–239. [CrossRef]
57. Zhou, Y.L.; Sun, X.M.; Zhang, R.H.; Zhu, Z.L.; Xu, J.P.; Li, Z.L. The improvement and validation of the model for retrieving the effective roughness length on TM pixel scale. In Proceedings of the IEEE International Geoscience and Remote Sensing Symposium, Seoul, Korea, 25–29 July 2005; pp. 3059–3062.